Minerva Bayesian Analysis of X-ray Imaging Spectrometer Data for Temperature and Density Profile Inference at Wendelstein 7-X

A. Langenberg[1], N.A. Pablant[2], O. Marchuk[3], D. Zhang[1], A. Alonso[4], R. Burhenn[1],

J. Svensson[1], P. Valson[1], D. Gates[2], M. Beurskens[1], R.C. Wolf [1], and the W7-X Team

[1] Max-Planck-Institut für Plasmaphysik, Greifswald, Germany

[2] Princeton Plasma Physics Laboratory, Princeton, NJ, USA

[3] Institut für Energie und Klimaforschung, Forschungszentrum Jülich GmbH, Jülich, Germany

[4] Laboratorio Nacional de Fusión – CIEMAT, 28040 Madrid, Spain

andreas.langenberg@ipp.mpg.de

Abstract. In the first operational phase of the stellarator Wendelstein 7-X (W7-X), the X-ray Imaging Crystal Spectrometer (XICS) system has been commissioned for measuring radial profiles of ion and electron temperature, T_i and T_e, plasma rotation velocities v_P, and selected impurity densities n_Z. This paper shows first measurements of the spectrometer and gives an initial calculation of impurity transport parameters derived from an Ar impurity transport study: Using the Minerva Bayesian analysis framework, the temporal evolution of Ar impurity density profiles after an Ar gas puff could be observed with a time resolution of up to 5 ms, yielding a maximum value for the diffusion coefficient of D = 1.5 m^2/s at ρ~0.5 and small pinch velocities in the inner plasma region.

1. Introduction

In the first operational phase of the stellarator W7-X, plasmas with peaked temperature profiles up to T_e = 8 keV and T_i = 2 keV and maximum pulse lengths of 6 s have been achieved. Based on the good performance, a rich physics program like the investigation of core electron root confinement [1,2], energy confinement [3], or impurity transport [4] have been realized. On the way towards a steady state operation of W7-X, the investigation of impurity transport is of particular interest. For stellarators, neoclassical theory predicts a general impurity inward drift which may lead to impurity accumulation in the plasma center and – in the worst case – to a potential plasma collapse due to impurity radiation, especially for long pulse times in the order of several minutes. Therefore, plasma scenarios preventing or minimizing impurity accumulation needs to be developed, using dedicated transport studies.

Impurity transport experiments have been performed successfully, injecting impurity species into the plasma and monitoring its temporal and/or radial redistribution, using several diagnostics [4-7]. A comparison of measured impurity abundances with simulated ones using various transport codes yields estimations on diffusive and convective transport coefficients.

In this paper, a method for the determination of transport coefficients directly from imaging spectrometer measurements without making use of transport code calculations is shown. The method relies on the measurement of neighbouring impurity charge states that together with its temporal evolution fully define the flux of one particular charge state. Here, calculations are done for Ar^{16+} (He-like argon), yielding initial observations of core transport coefficients in W7-X.

2. XICS Spectrometer Design

The X-ray Imaging Crystal Spectrometer XICS has been set up at W7-X in collaboration with the Princeton Plasma Physics Laboratory [8]. The spectrometer is equipped with a spherical bent crystal, imaging x-rays emitted from the plasma onto a two dimensional detector with energy resolution in horizontal, and spatial resolution in vertical direction. Fig.1 a) shows the designed viewing geometry of XICS with a spatial range covering radial positions $\rho = 0.84$ and $\rho = 0.42$ above and below the magnetic axis. Throughout this paper, ρ denotes the square root of normalized magnetic flux. Depending on the crystal choice and set Bragg angle, spectra of selected impurities, *e.g.* Ar, of a particular charge state can be monitored. Typical raw images for the emission of Ar^{16+} (*w*, *x, y,* and *z* lines) are shown in Fig.1 b), measured for a Bragg angle of 54.0° using a quartz crystal.

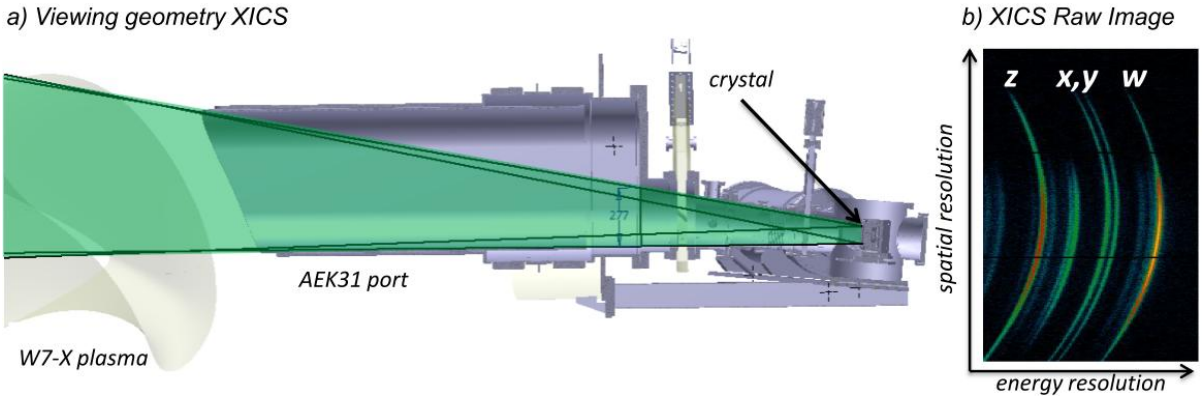

Fig.1. a) Viewing geometry of XICS diagnostic. b) Raw XICS detector image of Ar^{16+} emission.

3. Temperature and Density Profile Inference

A spectral fit of line of sight integrated spectra and a tomographic inversion of XICS data yields profiles of above mentioned plasma parameters as shown in Fig.2. Spectral fits (Fig.2(a), green lines) of measured data (Fig.2(a), blue lines) show an excellent match with deviations on the order of the photon statistics. From Doppler broadening and line intensity rations of the emission lines, line of sight integrated T_i and T_e values (blue and red dots in Fig.2 b) can be determined directly from the spectral fit.

The inference of actual temperature and density profiles has been done with an entire forward model of XICS using Bayesian Analysis for error estimation [9,10]. Thin gray solid lines in Fig.2 b) represent sampled profiles from the error distribution which yield forward modeled XICS data matching measured data within the photon statistics, the displayed error bars are the standard deviation of sampled profiles. The simultaneous fit of all emission lines in the spectra, including satellites from recombination and excitation of n_{Ar}^{15+} and n_{Ar}^{17+}, allows to infer n_{Ar}^{15+}, n_{Ar}^{16+}, and n_{Ar}^{17+} profiles (Fig.2b, green, red, and orange lines). Effects of charge exchange with the neutral H background gas have been neglected. We note the increase of the ratio between the z and the w line at the plasma edge. It is a strong indicator on the presence of neutrals [11] so that the diagnostic can be potentially used to derive the neutral density profile at the plasma edge. So for instance the increased ratio between n_{Ar}^{17+} to n_{Ar}^{16+} (Fig.2 b) towards the edge shows the role of the charge-exchange recombination in He-like spectra. All Ar densities are given in arbitrary units as an absolute density calibration is not available yet. However, the relative scaling of different charge states is accurate. The electron tempera-

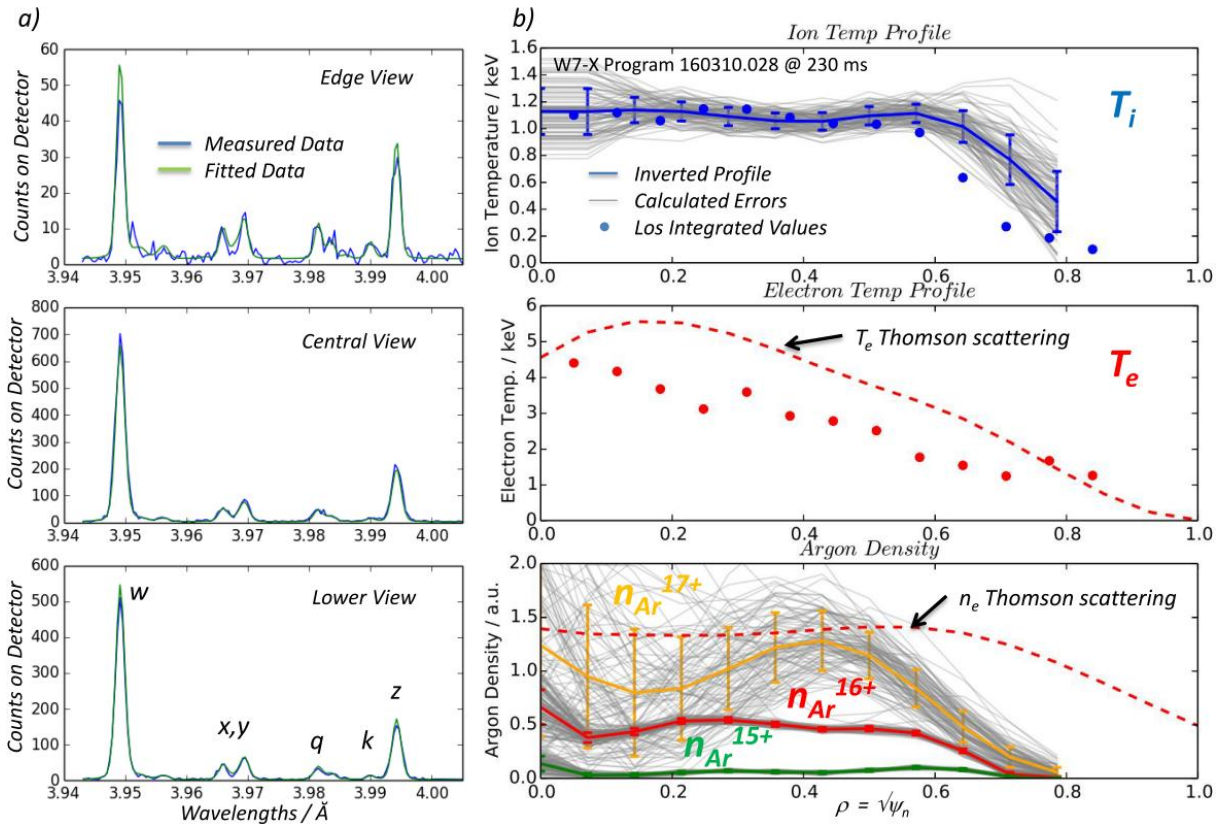

Fig.2. a) Measured and fitted XICS Ar^{16+} spectra along the outermost (edge and lower view) and the central line of sight. b) Inferred ion temperature (bold solid line) and Ar density profiles of different charge states (bold orange, red, and green lines) including calculated errors and profiles sampled from the error distribution (thin solid lines). Line of sight integrated temperature values are shown as dots.

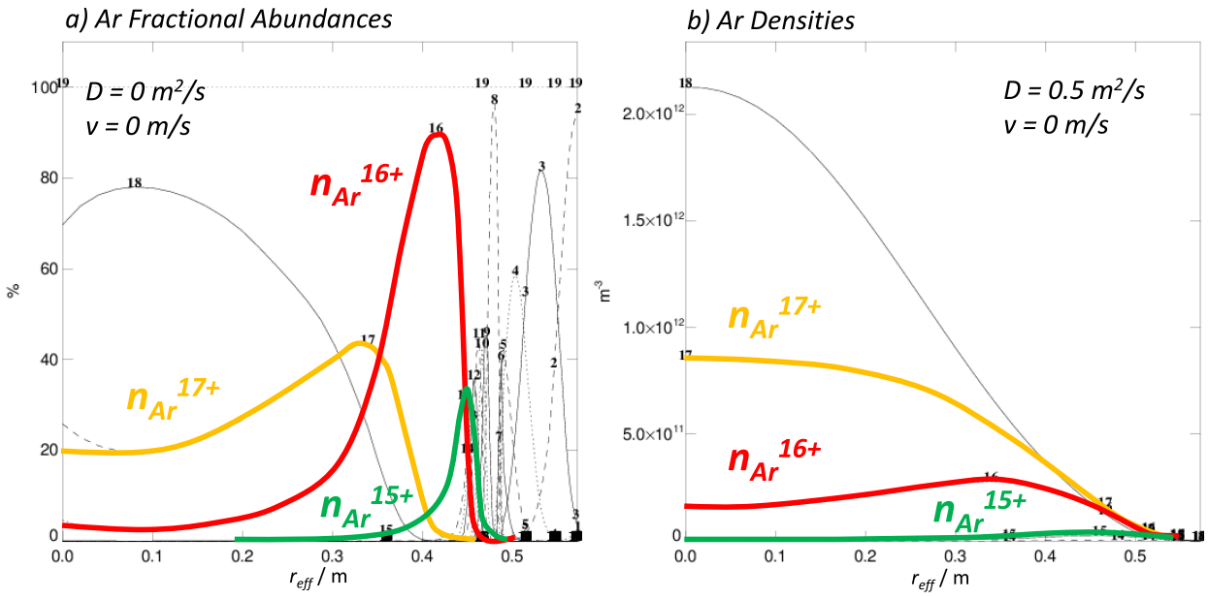

Fig.3. a) Fractional abundances of Ar for measured Te profile. b) Simulated Ar densities using a 1D STRAHL transport code.

ture and electron density profiles have been taken from Thomson scattering data (dashed lines in Fig.2b).

According to the fractional abundances of charge states at different T_e, Ar^{17+} is the dominant charge state for $T_e > 3$ keV, followed by Ar^{16+} and a small contribution from Ar^{15+}. Moreover, the penetration depth into the plasma center of n_{Ar}^{17+} and n_{Ar}^{16+} is significantly larger compared to n_{Ar}^{15+}.

For a first estimate of expected n_{Ar} profiles, Fig.3 a) shows fractional abundances of Ar in the coronal limit. Obviously, measured Ar profiles do clearly deviate from the coronal limit profiles, pointing out the influence of additional transport effects. In Fig.3 b), a 1D STRAHL [12] transport code calculation including transport effects has been carried out, using measured n_e and T_e profiles, assuming diffusion coefficients (D=0.5 m^2/s), and zero ion drift velocity as a first approach. The overall Ar profile shapes (compare Fig.2b) and 3b), including the intensity ratios between n_{Ar}^{15+}, n_{Ar}^{16+}, and n_{Ar}^{17+} profiles, can be resembled within the experimental uncertainties.

4. Argon Impurity Transport Study

For a more detailed analysis of impurity transport, Ar gas puff experiments have been performed. Therefore, a short Ar gas puff (30 ms) has been put into the plasma at a stationary phase with static Te and ne profiles, typically 150 ms after the start of the ECR heating. Fig.4 a)-c) shows the measured time dependent evolution of n_{Ar}^{15+}, n_{Ar}^{16+}, and n_{Ar}^{17+} profiles for t = 170-260 ms with a 5ms time resolution for the experiment program *160310.028*. Starting at 185 ms (35 ms after the Ar gas puff), a pronounced and fast rise of the Ar density profiles with a rise time of 30±5 ms can be observed, followed by a slow decay phase. A similar behavior can be observed for the n_{Ar}^{15+} and n_{Ar}^{17+} profiles.

The measured temporal evolution of n_{Ar}^{15+}, n_{Ar}^{16+}, and n_{Ar}^{17+} profiles are now used to calculate the Ar flux Γ_{Ar16+} of the particular charge state Ar16+ through:

$$\Gamma_{Ar16+} = -\frac{1}{r}\int_0^r \frac{\delta n}{\delta t}\, \acute{r}\, d\acute{r} + \frac{1}{r}\int_0^r Q\, \acute{r}\, d\acute{r} \qquad (1)$$

with the effective radius r in m, the time derivative of the n_{Ar}^{16+} density $\delta n/\delta t$, and the sinks and sources of n_{Ar}^{16+} given by recombination and ionization processes:

$$Q = n_e\left(S_{Ar15+} n_{Ar15+} - S_{Ar16+} n_{Ar16+} - R_{Ar16+} n_{Ar16+} + R_{Ar17+} n_{Ar17+}\right)$$

Here, S and R are ionization and recombination rate coefficients from ADAS database [13].

The flux $\Gamma_{dn/dt}$ associated to the time derivative of n_{Ar}^{16+} profiles (first term of Eq.1) is shown in Fig.4 d). Right after the Ar gas puff, $\Gamma_{dn/dt}$ profiles are negative until the n_{Ar}^{16+} profiles saturate, reflecting the penetration of Ar^{16+} into the plasma. For t > 230 ms, the n_{Ar}^{16+} density slowly decays, resulting in slightly positive $\Gamma_{dn/dt}$ flux profiles. Sink and source profiles (Fig.4 e) basically resemble the shapes of the Ar density profiles, with n_{Ar}^{16+} source terms (Q > 0) for ionization of Ar^{15+} and recombination of Ar^{17+} (green and orange profiles), and sinks (Q < 0) for ionization of Ar^{16+} (red profiles).

The corresponding total Ar^{16+} fluxes Γ_{Ar16+} can be parameterized by a diffusive and a convective contribution and have been normalized to n_{Ar}^{16+} and plotted versus the normalized

density gradients $\delta n/\delta r$ / n_{Ar}^{16+}, see Fig.4 f). A line fit yields the diffusive and convective transport coefficients D and v at the corresponding radial positions r according to

$$\Gamma_{Ar16+} = -D\frac{\delta n_{Ar16+}}{\delta r} + v n_{Ar16+}$$

Fig.5 shows the resulting D and v profiles for the Ar^{16+} charge state. The diffusion coefficient D rises from the plasma center towards larger plasma radii to a value of $D = (1.5 \pm 0.8)$ m^2/s

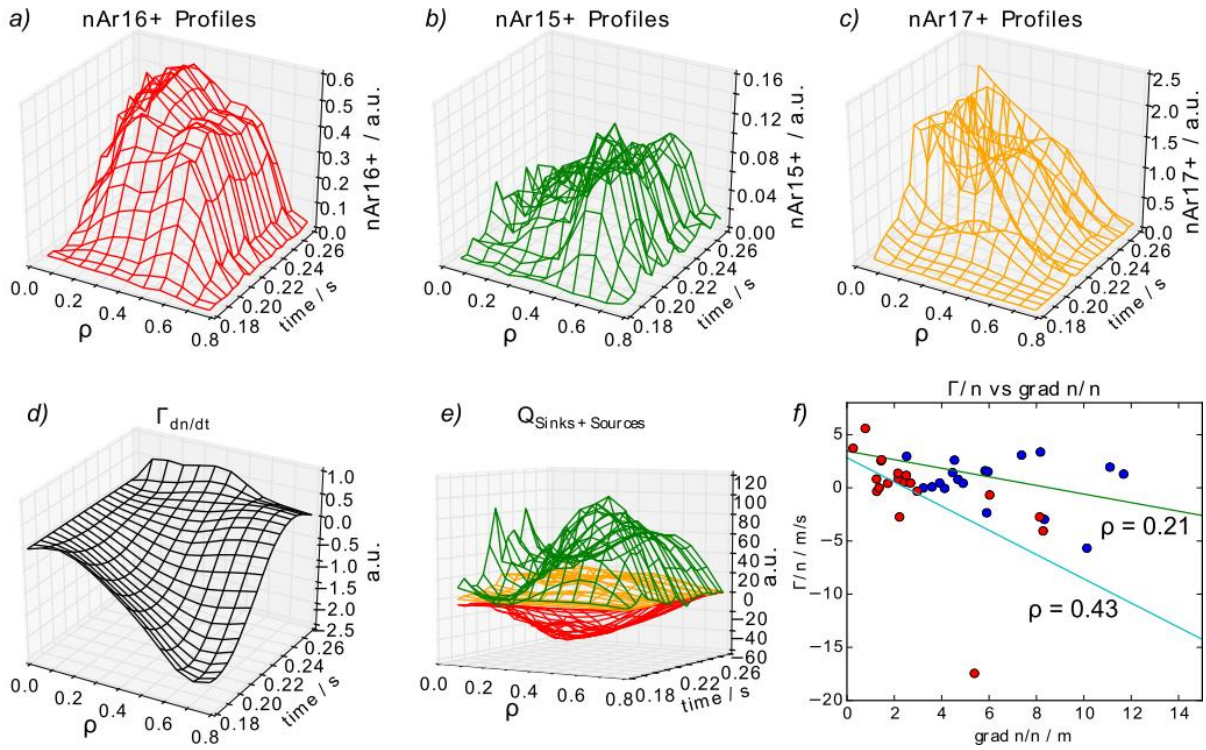

Fig.4. a)-c) Temporal evolution of measured n_{Ar}^{15+}, n_{Ar}^{16+}, and n_{Ar}^{17+} density profiles after an Ar gas puff. d) Temporal evolution of flux profiles of Ar^{16+} (neglecting sinks and sources). e) Sinks and sources for Ar^{16+} (see text). f) Normalized Ar^{16+} fluxes plotted versus normalized density gradients for effective radii of $\rho = 0.21$ and 0.43.

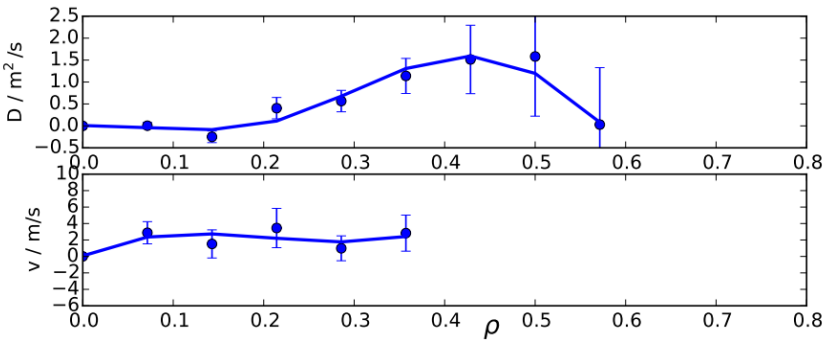

Fig.5. Inferred diffusive D and convective v transport coefficients for the Ar^{16+} transport.

at $\rho = 0.45$. Drift velocities v are close to zero with uncertainties of about ± 2 m/s. The statistics of inferred Ar profiles are too low for reasonable estimations of D at $\rho > 0.6$ and v at $\rho > 0.4$. However, inferred D and v profiles are in reasonable agreement with transport coefficients used for the above shown 1D STRAHL transport calculation, where constant profiles of $D = 0.5$ and $v = 0$ have been assumed (Fig3.b) for simplicity.

Improved statistics of measured XICS data and reduced uncertainties of inferred Ar profiles would allow a determination of the entire D and v profiles with much higher accuracies. For that purpose, several options like increasing the amount of puffed Ar in transport studies, binning of more spatial lines of sight, or a reduction of the time resolution are available and have not been optimized yet.

5. Summary

In this paper, an initial observation of the impurity transport coefficients D and v of the Ar^{16+} impurity charge state based on XICS measurements has been presented. The derived D and v profiles are in reasonable agreement with assumed transport coefficients of a 1D STRAHL transport code simulation.

Acknowledgments

This work has been carried out within the framework of the EUROfusion Consortium and has received funding from the Euratom research and training programme 2014-2018 under grant agreement No 633053. The views and opinions expressed herein do not necessarily reflect those of the European Commission.

[1] A. DINKLAGE *et al.* in 43rd EPS Conf. on Plasma Phys., Leuven (2016).

[2] N. PABLANT *et al.* in 43rd EPS Conf. on Plasma Phys., Leuven (2016).

[3] M. HIRSCH *et al.* in 26th IAEA Fusion Energy Conference, Kyoto (2016).

[4] A. LANGENBERG *et al.* in 43rd EPS Conf. on Plasma Phys., Leuven (2016).

[5] M. SERTOLI *et al.* Plasma Phys. Control. Fusion **53**, 035024 (2011).

[6] O. MARCHUK *et al.* Plasma Phys. Control. Fusion **48**, 1633 (2006).

[7] R. BURHENN *et al.* Fusion Sci. Technol. **46**, 115 (2004).

[8] N. PABLANT *et al.* in 41st EPS Conf. on Plasma Phys., 38F, 1.076, Berlin (2014).

[9] A. LANGENBERG *et al*. Fusion Sci. Technol. **69**, 560 (2016).

[10] J. SVENSSON *et al.* IEEE International Symp. on Intelligent Signal Processing, (2007).

[11] T. KATO *et al.* Phys. Rev. A, **44**, 6776 (1991).

[12] R. DUX, IPP report 10/30 (2006); K. BEHRINGER, JET report JET-R 87 08 (1987).

[13] http://open.adas.ac.uk/